RSC Advances

PAPER

View Article Online
View Journal | View Issue

Cite this: *RSC Adv.*, 2022, **12**, 12997

Nitrogen-doped mesoporous carbon supported CuSb for electroreduction of CO_2†

Yue Hou,[a] Cheng-Jie Jiang,[a] Ying Wang,[a] Jing-Wei Zhu,[a] Jia-Xing Lu *[ab] and Huan Wang *[ab]

Received 24th March 2022
Accepted 25th April 2022

DOI: 10.1039/d2ra01893d

rsc.li/rsc-advances

The construction of an efficient catalyst for electrocatalytic reduction of CO_2 to high value-added fuels has received extensive attention. Herein, nitrogen-doped mesoporous carbon (NMC) was used to support CuSb to prepare a series of materials for electrocatalytic reduction of CO_2 to CH_4. The catalytic activity of the composites was significantly improved compared with that of Cu/NMC. In addition, the Cu content also influenced the activity of electrocatalytic CO_2 reduction reaction. Among the materials used, the CuSb/NMC-2 (Cu: 5.9 wt%, Sb: 0.49 wt%) catalyst exhibited the best performance for electrocatalytic CO_2 reduction, and the faradaic efficiency of CH_4 reached 35%, and the total faradaic efficiency of C1–C2 products reached 67%.

Introduction

The huge combustion of fossil fuels such as coal, oil, and natural gas has led to a significant increase in the content of CO_2 in the atmosphere, causing serious ecological and environmental problems.[1–3] At the same time, CO_2 is also a rich and widely distributed potential carbon resource. However, CO_2 is a thermodynamically stable molecule, which makes it difficult to be reduced.[4] Among the various methods of utilization of CO_2, electrochemical method can be carried out at room temperature and atmospheric pressure.[5] Moreover, CO_2 can be converted into HCOOH, CO, alcohols or hydrocarbon products by different materials. Designing electrocatalysts with high faradaic efficiency (FE) and high stability is still a challenge.

Cu is considered to be an ideal CO_2 reduction electrode material due to its low cost and good catalytic performance compared with precious metals, such as Au[6] and Pd.[7] Moreover, Cu is the only metal electrocatalyst that can produce hydrocarbon in electrocatalytic CO_2 reduction reaction (CO_2RR), but its selectivity is poor.[8] Fortunately, modifying the Cu electrode by adding another metal can stabilize the intermediate and increase the selectivity of catalyst. Lee *et al.* believed that Cu surface-bound CO transfers to the second site may cause hydrogenation or additional C–C coupling.[9] Therefore, the Cu-based alloy catalyst has attracted widespread attention. Feng *et al.* prepared a homogeneous Cu–Zn alloy catalyst for the electrocatalytic CO_2RR, and a 33.3% FE of ethylene can be obtained at −1.1 V *vs.* RHE.[10] Su *et al.* synthesized hierarchically macroporous-mesoporous Cu/Zn alloys with two different pore diameters and adjustable alloy compositions. Through the synergistic effect of the hierarchical pore structure and the bimetallic elemental compositions, the electrocatalytic CO_2RR ability was significantly improved. The FE of ethanol reached 46.6% at −0.8 V *vs.* RHE and the catalyst had a stability of up to 11 h.[11] These studies show that Cu-based alloy catalyst is an effective catalyst for electrocatalytic CO_2RR with high selectivity.

On the other hand, mesoporous carbon materials have received widespread attention due to their large specific surface area, uniform and adjustable pore structure, stable chemical properties and high electrical conductivity.[12–15] Incorporating nitrogen into the mesoporous carbon material, due to the existence of nitrogen lone pair electrons, makes the originally neutral carbon material possess Lewis basicity, which is conducive to the adsorption of CO_2. Qin *et al.* used nitrogen-doped porous carbon for electrocatalytic CO_2RR, and a high FE of formate (68%) can be achieved at −0.86 V *vs.* RHE.[16] In addition, nitrogen can also form coordinate bond with metals to improve the stability of the supported catalyst.[17–19]

Based on these studies, a series of NMC supported CuSb catalysts (CuSb/NMC) for electrocatalytic CO_2RR were tailored and investigated in this work. By preparing materials with different Cu contents, the optimal CuSb/NMC catalyst was explored, and the FE of CH_4 reached 35%.

Results and discussion

CuSb/NMC composites were prepared by impregnation method (Fig. S1†), in which NMC precursor, $Cu(NO_3)_2 \cdot 3H_2O$ and $SbCl_3$ ethanol solution were mixed and then calcined at 500 °C under the atmosphere of N_2 (see the Experimental section for detail).

[a]*Shanghai Key Laboratory of Green Chemistry and Chemical Processes, School of Chemistry and Molecular Engineering, East China Normal University, Shanghai, 200062, China. E-mail: jxlu@chem.ecnu.edu.cn; hwang@chem.ecnu.edu.cn*

[b]*Institute of Eco-Chongming, Shanghai 202162, China*

† Electronic supplementary information (ESI) available: XRD, SEM, N_2 adsorption and desorption isotherms, and CVs. See https://doi.org/10.1039/d2ra01893d

The information about the morphology of materials can be obtained by scanning electron microscope (SEM) shown in Fig. 1 and S2,† and the particle diameter distribution histograms of materials are shown in Fig. S3.† The surface of NMC is flat and smooth (Fig. 1a). The surface morphologies of the substrate of CuSb/NMC, Cu/NMC and Sb/NMC catalysts are similar to those of NMC, which indicates that the combination of metals may not change the morphology of NMC. The metal particles of Cu/NMC (Fig. 1b) are clustered together. The interval with the largest particle number distribution of Cu/NMC is 127–161 nm (Fig. S3a†). The SEM image of Sb/NMC (Fig. 1c) shows a small number of particles. Compared with Cu/NMC, CuSb/NMC composites have better dispersion and smaller particles (Fig. 1d and S2†). The interval with the largest particle number distribution of CuSb/NMC-1, CuSb/NMC-2 and CuSb/NMC-3 is 70–85 nm, 70–85 nm and 85–100 nm, respectively (Fig. S3b–d†). According to the results of the particle size analysis, the particles of CuSb/NMC-1 and CuSb/NMC-2 composites possessed the similar size. Besides, due to a higher $Cu(NO_3)_2$ input, more nanoparticles are observed over the CuSb/NMC-2 (Fig. 1d) compared with those of the CuSb/NMC-1 (Fig. S2a†). The particles of CuSb/NMC-3 are larger than those of CuSb/NMC-2 (Fig. S3c and d†). It is possible that the increase of its loading leads to the aggregation of particles (Fig. S2b†), which might result in the low catalytic activity for CuSb/NMC-3.

X-ray diffraction (XRD) was used to characterize the crystalline phase structure of the composite materials, as shown in Fig. 2. The XRD pattern of NMC reveals one characteristic peak

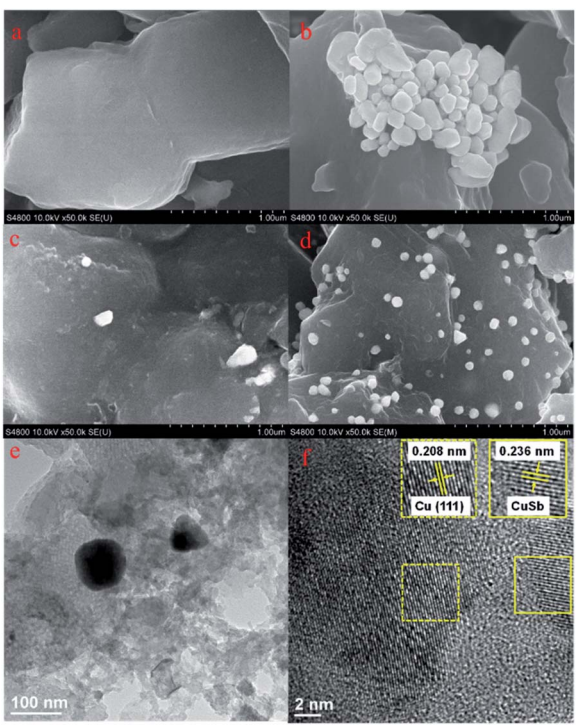

Fig. 1 SEM characterization results of materials (a) NMC, (b) Cu/NMC, (c) Sb/NMC, and (d) CuSb/NMC-2; and (e) TEM as well as (f) HR-TEM images of CuSb/NMC-2.

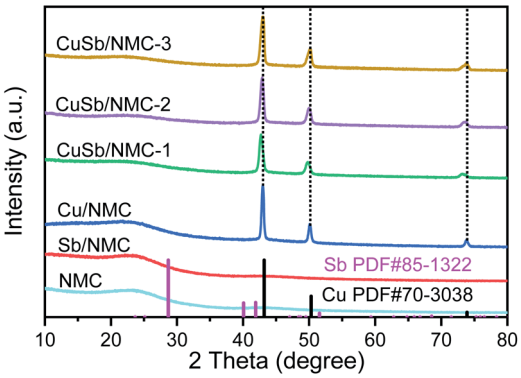

Fig. 2 XRD diffraction patterns of NMC, Cu/NMC, Sb/NMC and CuSb/NMC with different Cu contents.

at $2\theta = 23°$, which is attributed to the amorphous peak of NMC.[20,21] Cu/NMC have obvious peaks at $2\theta = 43.1°$, 50.2° and 73.8°, which are attributed to the (111), (200) and (220) crystal planes of Cu(0) according to PDF# 70-3038, respectively. It shows that Cu exists in the form of Cu^0 in Cu/NMC, and there is no Cu oxidation state species. No Sb-related diffraction peaks are detected in the XRD pattern of the Sb/NMC material, which might be due to the low Sb loading. Obvious diffraction peaks of Sb^0 could be detected with high Sb loading (Fig. S4†). The peak positions of CuSb/NMC are close to those of Cu/NMC, and slightly shifted to low angles. And, with the decrease of Cu/Sb ratio, this influence gradually increases. Therefore, it is speculated that Sb is doped into the crystal lattice of Cu to form CuSb alloy.[22] So CuSb/NMC is more dispersed than Cu/NMC (Fig. 1b and d).

The actual contents of Cu and Sb measured by inductively coupled plasma atomic emission spectroscopy (ICP-AES) are listed in Table 1. The loadings of Sb in Sb/NMC and CuSb/NMC composites are around 0.5 wt%. The Cu contents of CuSb/NMC-1, CuSb/NMC-2, CuSb/NMC-3 are 2.8 wt%, 5.9 wt% and 8.8 wt%, respectively. The content of Cu in Cu/NMC is 6.1 wt%.

The morphology of CuSb/NMC-2 was further observed by Transmission Electron Microscope (TEM). As it can be seen in Fig. 1e, the metal particles and carbon substrate can be facilely observed. Fig. 1f shows the characteristic Cu (111) facet with the lattice fringe of 0.208 nm. Besides, another particle with the lattice fringe of 0.236 nm was also observed, which may be caused by the doping of Sb.

Table 1 Textural and structural characteristics of composites

Sample	Cu loading[a] (wt%)	Sb loading[b] (wt%)	S_{BET}[c] ($m^2\ g^{-1}$)
NMC	—	—	460
Sb/NMC	—	0.51	461
Cu/NMC	6.1	—	433
CuSb/NMC-1	2.8	0.46	454
CuSb/NMC-2	5.9	0.49	432
CuSb/NMC-3	8.8	0.47	406

[a] Cu loading obtained by ICP. [b] Sb loading obtained by ICP. [c] S_{BET} Brunauer–Emmett–Teller (BET) surface area.

In order to determine the surface chemical composition of the CuSb/NMC composite, X-ray photoelectron spectroscopy (XPS) analysis was performed on the CuSb/NMC-2 material, and the results are shown in Fig. 3. It can be seen from the full spectrum (Fig. 3a) that there are five elements of C, O, N, Cu and Sb on the composite. Fig. 3b shows the Sb 3d spectrum and O 1s spectrum. The peaks of Sb $3d_{5/2}$ and Sb $3d_{3/2}$ (binding energy of 528.1 and 537.2 eV, respectively) clearly show that Sb exists in the form of Sb^0 in CuSb/NMC.[23] The O 1s at 530.8 eV can be assigned to the oxygen-containing groups in carbon skeleton.[24] Fig. 3c is the high-resolution Cu 2p spectrum of the material. There are two obvious characteristic peaks at 933.2 eV and 953.2 eV, which can be attributed to the characteristic Cu $2p_{3/2}$ and Cu $2p_{1/2}$.[25] Combined with the XRD characterization results, it shows that the Cu element in the material mainly exists in the form of Cu^0. It is worth noting that the binding energy (B.E.) of Sb $3d_{5/2}$ is negatively shifted by 0.2 eV compared with the standard B.E. (528.3 eV), while the B.E. of Cu $2p_{3/2}$ is shifted to a higher value (933.2 eV) compared to the standard B.E. (933.0 eV). These findings jointly indicate that there is an electronic shift from Cu to Sb, which is possibly originated from the doping of Sb into the Cu lattice. From the N 1s spectrum (Fig. 3d), it can be seen that there are two obvious characteristic peaks near 400.4 eV and 398.5 eV, which can be attributed to pyrrolic N and pyridine N, respectively.[22]

N_2 adsorption–desorption measurements were performed to explore the textural characteristics of the materials. It can be seen from Fig. S5a† that all materials show a typical mesoporous structure features–type-IV adsorption isotherm and type-H2 hysteresis loop. Fig. S5b† shows that NMC and composites have narrow pore size distribution of about 5 nm. The corresponding specific surface areas are listed in Table 1. It can be seen from Table 1 that the specific surface area of the pure NMC are 460 $m^2\ g^{-1}$. The specific surface area of Sb/NMC is not significantly different from that of NMC, which may be due to the low loading of Sb. The specific surface area of Cu/NMC decreases compared with that of NMC, which may be due to the high specific gravity of Cu.[26] For CuSb/NMC composites, with the increase of Cu content, the specific surface area of the material basically shows a downward trend. This phenomenon may be due to the increase of the specific gravity of Cu.

Linear sweep voltammetry (LSV) measurement was used to study the possibility of CuSb/NMC-2 as CO_2RR catalyst and compare the electrocatalytic activities of different materials. As shown in Fig. S6,† the current density under CO_2 atmosphere is higher than that under N_2 atmosphere, indicating that CuSb/NMC-2 is favorable for CO_2RR. The LSV curves of different materials under CO_2 atmosphere are shown in Fig. 4a, it can be seen that the electrochemical behaviors of different materials under CO_2 atmosphere are different. In the range of −0.8 V to −1.6 V *vs.* RHE, the current density of CuSb/NMC composites are higher than those of Cu/NMC, Sb/NMC and NMC materials, which indicates that the CuSb/NMC composites have higher catalytic activity of CO_2RR than Cu or Sb-supported material and pure NMC. Potentiostatic electrolysis was carried out at −1.46 V *vs.* RHE to investigate the electrocatalytic reduction ability of different materials, and the results are shown in Fig. 4b. When Sb/NMC and NMC were used as electrode materials, only H_2 was detected in gas products. When Cu/NMC was used as electrode material, CH_4, C_2H_4, CO and H_2 were

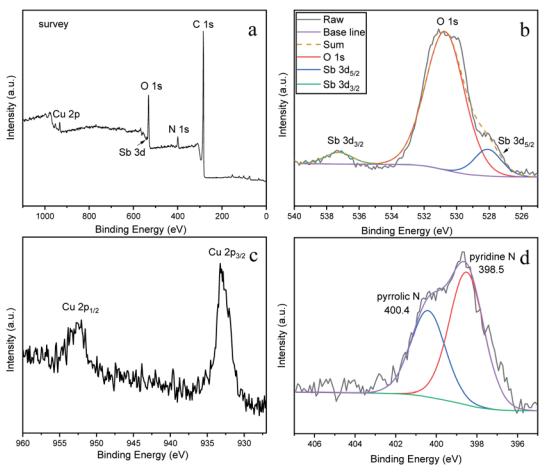

Fig. 3 (a) XPS survey spectrum, (b) Sb 3d spectrum and O 1s spectrum, (c) Cu 2p spectrum and (d) N 1s spectrum of CuSb/NMC-2.

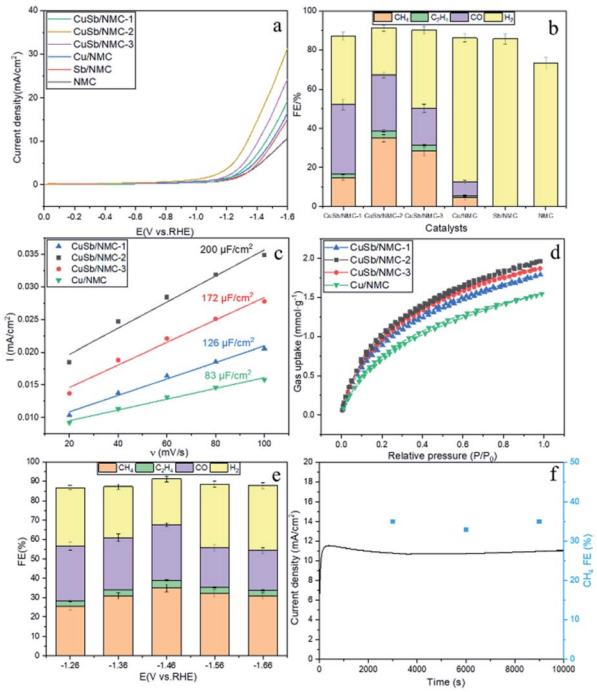

Fig. 4 (a) LSV curves of catalysts on glassy carbon electrode under saturated CO_2; (b) FEs of CO_2 reduction products of catalysts at −1.46 V *vs.* RHE in 0.1 M $KHCO_3$ solution saturated with CO_2; (c) the relationship between *I* and *ν* in CuSb/NMC composites and Cu/NMC; (d) CO_2 adsorption capacity of CuSb/NMC composites and Cu/NMC; (e) in the 0.1 M $KHCO_3$ solution, the FEs of CO_2 reduction products of different potentials on the CuSb/NMC-2 catalyst; (f) FE of CH_4 and current density over CuSb/NMC-2 electrode at −1.46 V *vs.* RHE within 10 000 s.

detected. Adding Cu to NMC for electrocatalytic CO_2RR can generate CH_4, C_2H_4 and CO, which indicating that Cu is the main active site of the CO_2RR. Interestingly, the FE of CH_4 over the CuSb/NMC composites was significantly higher than that over the Cu/NMC. Moreover, the hydrogen evolution reaction on CuSb/NMC composites is better suppressed than that on Cu/NMC. The high CO_2RR catalytic activity of the CuSb/NMC composites may be due to the electron shift from Cu to Sb that changes the electronic structure effect of the composites.

In order to investigate the influence of Cu content over the CuSb/NMC composites, the materials were tested by LSV measurement (Fig. 4a). The current density on CuSb/NMC-2 material was higher than those on the other two different CuSb/NMC materials with different Cu contents, showed obvious catalytic activity of CO_2RR. Moreover, under the potential of −1.46 V *vs.* RHE, the FE of CH_4 over the composites was greatly affected by the Cu content (Fig. 4b). With the increase of Cu content, the FE of CH_4 first increased and then decreased. The FE of C1–C2 products (CH_4, CO and C_2H_4) also increased first and then decreased. This may be because the addition of Cu affects the number of active sites. As shown by SEM images, too little Cu loading leads to fewer particles and active sites in the CuSb/NMC composite materials, while too much loading results in the aggregation of particles and thus reduces the active sites. Among all the materials, CuSb/NMC-2 exhibited the best catalytic performance for CH_4.

The larger electrochemical active surface area (ECSA), the more catalytically active sites can be provided for the electrocatalytic CO_2RR.[27] To check the ECSA of these materials, cyclic voltammograms in N_2-saturated 0.1 M $KHCO_3$ solution have been performed (Fig. S7†). The linear fitting diagram of the reduction current and the scanning rate of CuSb/NMC composites and Cu/NMC are shown in Fig. 4c. The C_{dl} of CuSb/NMC-1, CuSb/NMC-2, CuSb/NMC-3, Cu/NMC were 126 μF cm^{-2}, 200 μF cm^{-2}, 172 μF cm^{-2} and 83 μF cm^{-2}, respectively. The result of electrolysis corresponded to the C_{dl} of composites, which is positively correlated with ECSA. In general, the C_{dl} of CuSb/NMC composites were higher than that of Cu/NMC. It is possible that the particles of the composites are more dispersed due to the incorporation of Sb, which can be seen from the SEM characterization in Fig. 1 and S2,† thus their ECSAs are larger. For CuSb/NMC-1 and CuSb/NMC-2 materials, increasing the Cu content gradually increased the ECSA, which is beneficial to the electrocatalytic reduction of CO_2. The CuSb/NMC-2 had the largest ECSA. Thus, when the CuSb/NMC-2 was used as electrode material, the FE of CH_4 was the highest. When the Cu content continued to increase, the particles started to aggregate, which might result in minimally exposed electroactive sites and decreased the FE of CH_4. This result was also consistent with SEM.

Another important factor to improve the catalytic capacity of CO_2RR is the CO_2 adsorption capacity.[27–30] Therefore, CO_2 adsorption and desorption tests were performed on the materials (Fig. 4d). CuSb/NMC composites showed a higher adsorption capacity of CO_2 than Cu/NMC. Among a series of materials with different Cu contents, CuSb/NMC-2 had the highest CO_2 adsorption capacity, which may be beneficial for electrocatalytic CO_2RR.

In order to explore the influence of electrolytic potential, CuSb/NMC-2, the optimal catalyst previously explored, was used as electrode material for CO_2 potentiostatic electrolysis. It can be seen from Fig. 4e that with the negative shift of the potential, the FE of CH_4, C_2H_4 and CO reached the maximum at −1.46 V *vs.* RHE (35%, 3% and 29%, respectively), and then the FE of CH_4 and CO decreased due to the more intense hydrogen evolution reaction. A suitable negative shift of potential can provide sufficient energy for the reaction, thus facilitating electrocatalytic CO_2RR. Therefore, −1.46 V *vs.* RHE was the optimal reaction potential. When the potential is too negative, the hydrogen evolution reaction is intense, which is not conducive to the electrocatalytic CO_2RR.

The stability of the optimal material CuSb/NMC-2 was tested by electrolysis at the optimal potential (−1.46 V *vs.* RHE) for a long time. In the process of electroreduction, the current density shows an upward trend within 300 s and then stabilizes at 11 mA cm^{-2} within 10 000 s without obvious change (Fig. 4f). The FE of CH_4 does not change significantly and remains around 35%. The electrolytic material was characterized by SEM and XRD, and the results are shown in Fig. S8.† As can be seen from the SEM diagram of the material in Fig. S8a,† no obvious agglomeration occurred in the material after electrolysis. As can be seen from the XRD characterization of the material in Fig. S8b,† the peak positions of the material before and after electrolysis did not change, indicating that the material has good stability.

Conclusions

In short, we have synthesized a series of materials with different Cu contents for electrocatalytic reduction of CO_2 to CH_4. Compared with Cu/NMC, Sb/NMC and NMC, CuSb/NMC exhibits excellent electrocatalytic performance of CO_2RR. CuSb/NMC-2 has the best catalytic performance, and the FE of CH_4 (35%) is 7 times that of Cu/NMC. The introduction of Sb facilitated the dispersion of particles, inhibited their agglomeration and increased the catalytic active sites.

Experimental

Materials

3-Amino phenol (A.R.), hexamethylene tetramine (A.R.), $Cu(NO_3)_2 \cdot 3H_2O$ (A.R.), $SbCl_3$ (A.R.), ethanol (A.R.) and $KHCO_3$ (A.R.) were purchased from Sinopharm Chemical Reagent Co. Ltd; F127 (Shanghai Aladdin Reagents Co. Ltd); Nafion® 117 solution (5%, Dupont); Nafion 117 membrane (Dupont); Carbon paper (CP, HCP010, Shanghai Hesen Electrical Co. Ltd); CO_2 and N_2 (99.99%, Shanghai Dumaoai Purifying Gas Co. Ltd).

Characterization

XRD patterns were recorded using an Ultima IV X-ray powder diffractometer equipped with Cu Kα radiation (k = 1.5406 Å). The values for actual Cu and Sb loads of the synthesized

catalysts were determined on an inductively coupled plasma atomic emission spectroscopy (ICP-AES, IRIS Intrepid II XPS, Waltham, MA, USA). XPS analysis was performed on the Thermo Scientific ESCA Lab 250Xi using 200 W monochromatic Al Kα radiation. The 500 mm X-ray spot was used. The base pressure in the analysis chamber was about 3×10^{-10} mbar. SEM morphology of the samples was characterized using a Hitachi S4800 scanning electron microscope at 10 kV. TEM images were recorded by TECNAI G2F30 transmission electron microscope. Nitrogen adsorption–desorption isotherms and BET surface areas were measured with a Belsorp-Max analyzer at 77 K. The adsorption isotherms of CO_2 were determined at 25 °C with a Belsorp-Max analyzer. All the electrochemical experiments were performed using a CHI650A electrochemical station (Shanghai Chenhua Instrument Co. Ltd).

Materials synthesis

The NMC precursor was synthesized by the method previously reported in the literature.[22] The synthesis procedure of CuSb/NMC is shown in Fig. S1.† Typically, 0.5 g of NMC precursor was dispersed in 25 mL of ethanol. Subsequently, 0.1 g of $Cu(NO_3)_2 \cdot 3H_2O$ and 4.3 mL of 5 mM $SbCl_3$ ethanol solution were successively added to the NMC precursor dispersion and stirred for 4 h. After that, the solvent was removed by rotary evaporation at 40 °C. The resulting solid was heated to 500 °C with a rate of 1 °C min^{-1} and kept at that temperature for 3 h under the atmosphere of N_2. The material obtained after calcination was named as CuSb/NMC-2. By adjusting the amount of $Cu(NO_3)_2 \cdot 3H_2O$ to 0.08 g and 0.12 g, CuSb/NMC-1 and CuSb/NMC-3 were also prepared. Moreover, Cu/NMC and Sb/NMC were prepared using the same process, except for the absence of $SbCl_3$ ethanol solution or $Cu(NO_3)_2 \cdot 3H_2O$, respectively.

Electrochemical study

In order to prepare the CuSb/NMC electrode, 2 mg of the CuSb/NMC material prepared above was ultrasonically dispersed in 40 μL of deionized water and 20 μL of Nafion 117 dispersion (5 wt%) to form a homogeneous solution. The resulting solution was coated on the surface of the carbon paper with a pipette, and then dried at room temperature. The coating amount of catalyst was 0.6 mg cm^{-2}.

The electrolysis experiment was carried out in an H-type electrolytic cell separated by a Nafion 117 proton exchange membrane at 25 °C with a CuSb/NMC electrode as the cathode, a Pt mesh electrode as the anode and a saturated calomel electrode (SCE) as the reference electrode. A 0.1 M $KHCO_3$ solution saturated with CO_2 was used as electrolyte. Then the potentiostatic electrolysis was carried out at the same CO_2 bubble rate of 0.01 L min^{-1}.

LSV measurement was performed within a single chamber electrolytic cell with a three-electrode system, which included a working electrode (CuSb/NMC catalyst coated on a glassy carbon electrode, the coating amount of catalyst was also 0.6 mg cm^{-2}), a Pt mesh electrode and an SCE reference electrode. A 0.1 M $KHCO_3$ solution was used as the electrolyte, and N_2 or CO_2 was introduced for at least 30 minutes to form a N_2- or CO_2-saturated solution (pH 8.57 and 6.80, respectively). The scanning rate is 50 mV s^{-1}. To avoid the effect of solution pH, all potentials were converted to potentials relative to the reversible hydrogen electrode by formula (1). The vertical coordinate current density of the LSV curve is determined by dividing the current value by the geometric area. The reduction current is set to be positive.

$$E(vs.\ \mathrm{RHE}) = E(vs.\ \mathrm{SCE}) + 0.0591\ \mathrm{V} \times \mathrm{pH} + 0.241\ \mathrm{V} \quad (1)$$

The experimental device, electrode processing and preparation of electric double layer capacitance test were consistent with the LSV measurement experimental device. 0.1 M $KHCO_3$ solution saturated with N_2 was used as the electrolyte, and 20 mV s^{-1}, 40 mV s^{-1}, 60 mV s^{-1}, 80 mV s^{-1}, and 100 mV s^{-1} were selected in the potential range of the non-Faraday current (0.75–0.35 V *vs.* RHE) for cyclic voltammetry, the formula is as follows, where I is the current density, calculated by dividing the current value by the geometric area.

$$C_{\mathrm{dl}} = \frac{I}{\nu} \quad (2)$$

Product analysis

The gas product was detected by a gas chromatograph (GC; Agilent 7890) equipped with a flame ionization detector to detect hydrocarbons and a thermal conductivity detector to detect H_2 and CO. The liquid product was qualitatively detected by GC-2014C with HS-9A headspace injection. The Faraday efficiency of gas phase products was calculated by the following formula:

$$\mathrm{FE} = \frac{\phi v t Z F}{Q V_{\mathrm{m}}} \times 100\% \quad (3)$$

where φ is the volume fraction of gaseous products. v is the flow rate of CO_2 gas (v = 0.01 L min^{-1}). t is the electrolysis time (min). Z is the number of electrons transferred to the product (when the product is H_2 and CO, $Z = 2$; when the product is CH_4, $Z = 8$; when the product is C_2H_4, $Z = 12$). F is Faraday's constant, which is 96 500C mol^{-1}. Q is the total quantity (C) of electric charge, used by the cell during the overall electrolysis process. V_{m} is the molar volume of gas at 298.15 K, 101 kPa, and its value is 24.04 L mol^{-1}.

Conflicts of interest

There are no conflicts to declare.

Acknowledgements

This project was supported by National Key R&D Program of China (2020YFA0710200) and National Natural Science Foundation of China (22072046).

Notes and references

1 W. Ma, S. Xie, T. Liu, Q. Fan, J. Ye, F. Sun, Z. Jiang, Q. Zhang, J. Cheng and Y. Wang, *Nat. Catal.*, 2020, **3**, 478–487.
2 A. X. Guan, Z. Chen, Y. L. Quan, C. Peng, Z. Q. Wang, S. K. Sham, C. Yang, Y. L. Ji, L. P. Qian, X. Xu and G. F. Zheng, *ACS Energy Lett.*, 2020, **5**, 1044–1053.
3 A. Liu, M. Gao, X. Ren, F. Meng, Y. Yang, L. Gao, Q. Yang and T. Ma, *J. Mater. Chem. A*, 2020, **8**, 3541–3562.
4 X. Ba, L.-L. Yan, S. Huang, J. Yu, X.-J. Xia and Y. Yu, *J. Phys. Chem. C*, 2014, **118**, 24467–24478.
5 J. Yuan, L. Liu, R. R. Guo, S. Zeng, H. Wang and J. X. Lu, *Catalysts*, 2017, **7**, 220–231.
6 C. G. Morales-Guio, E. R. Cave, S. A. Nitopi, J. T. Feaster, L. Wang, K. P. Kuhl, A. Jackson, N. C. Johnson, D. N. Abram, T. Hatsukade, C. Hahn and T. F. Jaramillo, *Nat. Catal.*, 2018, **1**, 764–771.
7 R. Kortlever, I. Peters, S. Koper and M. T. M. Koper, *ACS Catal.*, 2015, **5**, 3916–3923.
8 S. Nitopi, E. Bertheussen, S. B. Scott, X. Liu, A. K. Engstfeld, S. Horch, B. Seger, I. E. L. Stephens, K. Chan, C. Hahn, J. K. Norskov, T. F. Jaramillo and I. Chorkendorff, *Chem. Rev.*, 2019, **119**, 7610–7672.
9 C. W. Lee, K. D. Yang, D. H. Nam, J. H. Jang, N. H. Cho, S. W. Im and K. T. Nam, *Adv. Mater.*, 2018, **30**, e1704717.
10 Y. Feng, Z. Li, H. Liu, C. Dong, J. Wang, S. A. Kulinich and X. Du, *Langmuir*, 2018, **34**, 13544–13549.
11 X. Su, Y. Sun, L. Jin, L. Zhang, Y. Yang, P. Kerns, B. Liu, S. Li and J. He, *Appl. Catal., B*, 2020, **269**, 118800–118808.
12 Z. U. Ahmad, L. Yao, J. Wang, D. D. Gang, F. Islam, Q. Lian and M. E. Zappi, *Chem. Eng. J.*, 2019, **359**, 814–826.
13 V. S. gharahshiran and M. Yousefpour, *Int. J. Hydrogen Energy*, 2018, **43**, 7020–7037.
14 N. Sahin, W. O. Silva, M. R. Camilo, E. A. Ticianelli, F. H. B. Lima, J. Parmentier, C. Comminges, T. W. Napporn and K. B. Kokoh, *Sustainable Energy Fuels*, 2020, **4**, 6045–6053.
15 X. Wang, M. Qiu, R. L. Smith, J. Yang, F. Shen and X. Qi, *ACS Sustainable Chem. Eng.*, 2020, **8**, 18157–18166.
16 Z. Qin, X. Jiang, Y. Cao, S. Dong, F. Wang, L. Feng, Y. Chen and Y. Guo, *Sci. Total Environ.*, 2020, **759**, 143575–143582.
17 Y. Guo, J. He, T. Wang, H. Xue, Y. Hu, G. Li, J. Tang and X. Sun, *J. Power Sources*, 2011, **196**, 9299–9307.
18 S.-H. Liu, M.-T. Wu, Y.-H. Lai, C.-C. Chiang, N. Yu and S.-B. Liu, *J. Mater. Chem.*, 2011, **21**, 12489–12496.
19 Z. Lei, L. An, L. Dang, M. Zhao, J. Shi, S. Bai and Y. Cao, *Microporous Mesoporous Mater.*, 2009, **119**, 30–38.
20 X. Peng, Y. Mi, H. Bao, Y. Liu, D. Qi, Y. Qiu, L. Zhuo, S. Zhao, J. Sun, X. Tang, J. Luo and X. Liu, *Nano Energy*, 2020, **78**, 105321–105326.
21 S. Gao, Y. Liu, Z. Xie, Y. Qiu, L. Zhuo, Y. Qin, J. Ren, S. Zhang, G. Hu, J. Luo and X. Liu, *Small Methods*, 2021, **5**, 2001039–2001044.
22 G. H. Wang, Z. Cao, D. Gu, N. Pfander, A. C. Swertz, B. Spliethoff, H. J. Bongard, C. Weidenthaler, W. Schmidt, R. Rinaldi and F. Schuth, *Angew. Chem., Int. Ed.*, 2016, **55**, 8850–8855.
23 H. Li, T.-W. Jiang, X. Qin, J. Chen, X.-Y. Ma, K. Jiang, X.-G. Zhang and W.-B. Cai, *ACS Catal.*, 2021, **11**, 6846–6856.
24 X. Wan, Y. Li, H. Xiao, Y. Pan and J. Liu, *RSC Adv.*, 2020, **10**, 2932–2941.
25 D.-M. Wang, A.-C. Miller and M.-R. Notis, *Surf. Interface Anal.*, 1996, **24**, 127–132.
26 J.-J. Zhang, S.-L. Shan, Y. Shi, Y. Hou, H. Wang and J.-X. Lu, *J. Electroanal. Chem.*, 2021, **882**, 114962–114970.
27 J. Yuan, M.-P. Yang, W.-Y. Zhi, H. Wang, H. Wang and J.-X. Lu, *J. CO_2 Util.*, 2019, **33**, 452–460.
28 S. Gao, Y. Lin, X. Jiao, Y. Sun, Q. Luo, W. Zhang, D. Li, J. Yang and Y. Xie, *Nature*, 2016, **529**, 68–71.
29 S. Liu, X. F. Lu, J. Xiao, X. Wang and X. W. D. Lou, *Angew. Chem., Int. Ed.*, 2019, **58**, 13828–13833.
30 S. Liu, J. Xiao, X. F. Lu, J. Wang, X. Wang and X. W. D. Lou, *Angew. Chem., Int. Ed.*, 2019, **58**, 8499–8503.